CYCLONE GLOBAL NAVIGATION SATELLITE SYSTEM (CYGNSS)

Algorithm Theoretical Basis Document	UM Doc. No.	148-0137
Level 1B DDM Calibration	SwRI Doc. No.	N/A
	Revision	3
	Date	20 Oct 2020
	Contract	NNL13AQ00C

Algorithm Theoretical Basis Documents (ATBDs) provide the physical and mathematical descriptions of the algorithms used in the generation of science data products. The ATBDs include a description of variance and uncertainty estimates and considerations of calibration and validation, exception control and diagnostics. Internal and external data flows are also described.

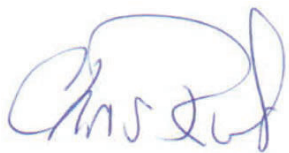# CYCLONE GLOBAL NAVIGATION SATELLITE SYSTEM (CYGNSS)

Algorithm Theoretical Basis Document	UM Doc. No.	148-0137
Level 1B DDM Calibration	SwRIDoc. No.	N/A
	Revision	2
	Date	10 Oct 2020
	Contract	NNL13AQ00C

Prepared by Scott Gleason, 22 October 2020

Approved
by:

Chris Ruf, CYGNSS Principal Investigator

Date: 23 Oct 2020

Approved
by:

Tim Butler, CYGNSS SOC Manager

Date: 24 Oct 2020

Released
by:

Darren McKague, CYGNSS UM Project Manager

Date:

October 23, 2020

REVISION NOTICE

Document Revision History		
Revision	**Date**	**Changes**
PRE-RELEASE DRAFT	17 June 2013	n/a
INITIAL RELEASE	14 January 2014	Add unwrapping of the radar range equation to estimate normalized scattering cross-section from received power. Add detailed error analysis.
Rev 1	19 December 2014	Change L1b DDM units to scattering cross-section in meters2. Add ancillary data product of scattering area in each DDM bin. Add greater detail about algorithm implementation.
Rev 2	20 August 2018	Inclusion of all modifications made to the Level 1A algorithms based on observed on-orbit performance between March 2017 and August 2018.
Rev 3	20 October 2020	Inclusion of all modifications for for zenith EIRP calibration.

Contents

I. LEVEL 1B CALIBRATION APPROACH

This document is the second part of the overall Level 1 Calibration Algorithm Theoretical Basis Document (ATBD) describing the Level 1b calibration. Portions of this ATBD have been re-published in [1].

The Level 1b calibration is performed after the Level 1a calibration and will use external meta-data to convert the Level 1a mapped power in Watts to a delay Doppler map (DDM) map of normalized bistatic radar cross section (NBRCS) values. This conversion will be done for every pixel in every DDM and requires the following information at the time the science DDM is collected,

1) The CYGNSS satellite GPS time, position and velocity in the WGS84 Earth Centered Earth fixed (ECEF) reference frame.
2) The GPS satellite position and velocity in the Earth WGS84 Centered Earth fixed (ECEF) reference frame.
3) Detailed knowledge of the CYGNSS nadir antenna gain patterns.
4) Best estimated attitude knowledge of the CYGNSS spacecraft at the time of the measurement.
5) An estimate of the GPS effective isotropic radiative power (EIRP) in the direction of the specular reflection point in the GPS satellite reference frame.

Additional information calculated using the per DDM science meta data and used in the Level 1b calibration of each
DDM includes,

1) An accurate surface geolocation of the reflection specular point (SP) in the WGS84 ECEF reference frame.
2) A precise estimate of the specular reflection point location in the measurement DDM pixel delay and Doppler bins.
3) The path length between the GPS satellite and specular reflection point and between the specular reflection point and the CYGNSS spacecraft making the measurement.
4) The effective scattering area per DDM bin surrounding the specular point over all delay and Doppler bins.

The above parameters are then used to estimate values of the bistatic radar cross section for each DDM pixel using the forward model described below.

II. FORWARD MODEL OF SCATTERED SIGNAL POWER

A full expression for the GPS scattered signal power has been previously derived and published in 2000 [2], shown in Equation 1. The original representation has been slightly modified in form and variable names,

$$P^g_{\hat{\tau},\hat{f}} = \frac{P^T \lambda^2}{(4\pi)^3} \iint_A \frac{G^T_{x,y} \sigma^0_{x,y} G^R_{x,y}}{(R^R_{x,y})^2 (R^T_{x,y})^2} \Lambda^2_{\hat{\tau};x,y} S^2_{\hat{f};x,y} dxdy$$

(1)

where $P^g_{\hat{\tau},\hat{f}}$ is the coherently processed scattered signal power, in Watts. P^T is the GPS satellite transmit power and $G^T_{x,y}$

is the GPS satellite antenna gain. $G^R_{x,y}$ is the CYGNSS satellite receiver antenna gain. $R^T_{x,y}$ and $R^R_{x,y}$ are the transmitter to surface and surface to receiver ranges, respectfully. $\sigma_{x,y}{}^0$ is the normalized bistatic scattering cross section (NBRCS). λ is the GPS signal carrier wavelength (approx. 19 cm). $\Lambda_{\hat{\tau};x,y}$ is the GPS signal spreading function in delay and $S_{\hat{f};x,y}$ is the frequency response of the GPS signal. A is the surface integration area covering the effective region of diffuse scattering for each delay Doppler bin. The scattered signal power is processed using a 1ms coherent integration intervals over a range of relative delays $\hat{\tau}$ and Doppler frequencies $\hat{f}$, followed by 1 second of non-coherent averaging. These delay and frequency bins map non-uniquely spatially to physical coordinates on the surface.

The above expression can be simplified using the effective values of several variables across delay and Doppler bins under the integrand of Equation 1. The effective values include the effects of delay and Doppler spreading functions, Λ and S, which have been eliminated from the Equation and are indicated by the over-bar in the following equations. The surface mapping from physical (x,y) coordinates to delay and Doppler coordinates reflects the actual processing as performed in the CYGNSS delay Doppler mapping instrument (DDMI).

$$P^g_{\hat{\tau},\hat{f}} = \frac{P^T \lambda^2 G^T_{\hat{\tau},\hat{f}} <\sigma^0_{\hat{\tau},\hat{f}}> \bar{G}^R_{\hat{\tau},\hat{f}} \bar{A}_{\hat{\tau},\hat{f}}}{(4\pi)^3 (\bar{R}^R_{\hat{\tau},\hat{f}})^2 (\bar{R}^T_{\hat{\tau},\hat{f}})^2}$$

(2)

where, $\bar{G}^R_{\hat{\tau},\hat{f}}=$ The effective receiver antenna gain at each delay/Doppler bin. $\bar{R}^T_{\hat{\tau},\hat{f}}$ and $\bar{R}^R_{\hat{\tau},\hat{f}}$ are the effective range losses at each delay/Doppler bin and $\bar{A}_{\tau,\hat{f}}$ is the effective surface scattering area at each delay/Doppler bin.

All variables in Equation 2 vary with respect to delay $\hat{\tau}$ and Doppler $\hat{f}$ (which map to the x,y surface grid over the glistening zone), however, for the sake of simplification and with negligible loss in accuracy, several parameters can be estimated and applied as constants across the DDM measurement as expressed below.

III. GEOLOCATION OF SURFACE MEASUREMENT: SOLVING FOR THE SURFACE SPECULAR REFLECTION POINT

The estimated location of the center of the surface glistening zone of the reflected signal provides the main point of reference for the geo-location of the GNSS-R measurement. This point on the surface is referred to as the specular point and can be estimated mathematically using the physical geometry of the transmitting and receiving satellites and a modeled of the Earth's ocean surface. It should be noted that the surface specular point estimation algorithm described below is designed for ocean surfaces. Land specular points over varying topography present unique challenges and will contain additional geolocation errors, not yet accounted for in the current CYGNSS Level 1 calibration.

In the original Level 1 calibration approach, the specular point was solved using a) the position of the receiving satellite, as estimated by the 1Hz single frequency position estimate, b) the estimate of the transmitting satellite using ground based precise ephemeris and c) the WGS84 ellipsoid model of the Earth. This Earth model, although generally accurate enough for most applications, relied on approximations that resulted in residual specular point position estimation errors that where large enough to significantly impact the pixels in the DDM used to calculated the bistatic radar cross section. Subsequently, an improved specular point solver was implemented that used a more accurate DTU10

mean sea surface model [3], combined with a brute force, computationally-efficient specular point solver algorithm.

The specular point on the Earth maps to a single point in the delay-Doppler coordinates in the CYGNSS DDM. The exact specular bin location in the DDM will be located at a fractional pixel location within a single DDM bin. The pixels in the DDM at and surrounding the specular point bin determine the region used to make the surface bistatic radar cross section measurement, the DDMA. The estimation of the DDMA within the Level 1a DDM is described in more detail below using the precise location of the specular point described here. This region of the DDM represents the bins of highest reflected power and smallest spatial footprint on the surface and accurate knowledge of this regions is critical for calibration and wind speed retrievals.

The specular point location on the surface can't be reliably estimated using the peak power bin of the DDM. The peak power pixel results from a combination of effects in addition to the specular point location, including thermal noise, speckle noise or asymmetries in the reflected signal waveform (as a result of geometry and antenna pattern non-uniformity). For this reason, the specular point surface location and location of the specular point in the instrument generated DDM is calculated to a sub-pixel level from first principles (i.e. geometry and timing metadata).

A. Mean Sea Surface Height Model

In order to more precisely predict the specular location, it is necessary to account for deviations in the Earth's mean sea surface height as compared to the WGS84 model. For this purpose, we have utilized the DTU10 mean sea surface model [3]. The mean sea surface is the displacement of the sea surface relative to a mathematical model of the Earth and it closely follows the Earth's geoid. The amplitude of the deviation from the WGS84 ellipsoid is generally within approximately +/100 meters over the Earth's ocean surfaces. The original DTU10 data was reduced to a 1 degree by 1 degree resolution to improve the efficiency of the calculation, and which is reasonable, due to the fact that height variations are relatively small. The DTU10 map of sea surface height variations relative to the WGS84 ellipsoid use in the specular point solver is shown in Figure 1.

The path delay error manifests itself as an error in the predicted reflection path delay, which, in turn, becomes an error in the predicted location of the specular bin in the DDM. The error in predicted path delay can be expressed as,

$$\rho = 2\cos(\theta)\delta h \qquad (3)$$

Where ρ is the path delay error, θ is the reflection incidence angle and δh is the relative surface height error with respect to the WGS84 ellipsoid.
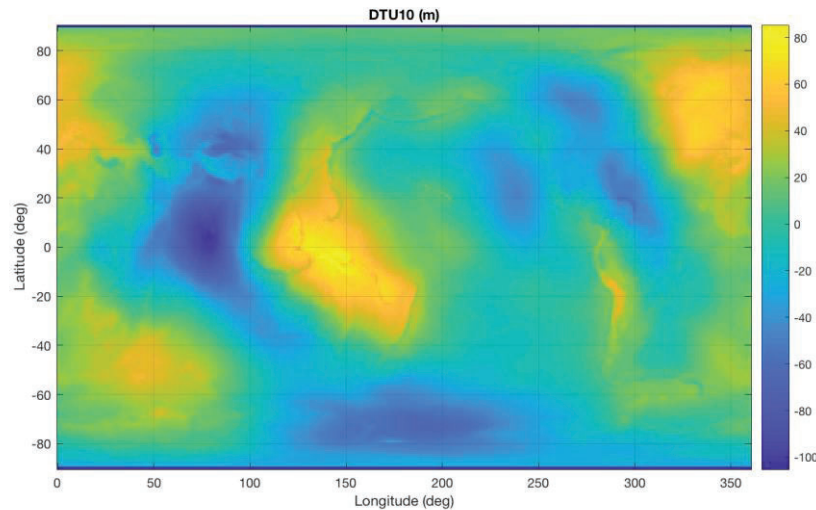
5

Fig. 1.DTU10 Mean Sea Surface data used for specular point calculation.

The height difference, manifests as a path delay error which becomes an error in the predicted location of the specular bin in the DDM. For a typical incidence angle of 30 degrees, a surface height error of 100 meters could result in 170 meters of path delay error. In the CYGNSS DDM, the delay pixel resolution is approximately 0.25 GPS L1 C/A code chips, and one chip corresponds to approximately 293 meters of delay. Therefore, a 170 m path delay error results in the predicted specular bin in the DDM being offset by 2.25 pixels from where we would expect it on the WGS84 ellipsoid.

Figure 2 shows a plot of specular bin delay difference when using DTU10 as opposed to using WGS84. Specular delay differences are shown for 1 day of measurements for 4 satellites (each shown in 4 separate colors). We can observe that the delay difference (or correction) due to the improved specular point solver varies between -2 and 2.5 pixels in delay space in the DDM. Figure 2 also shows an example measured CYGNSS DDM. In the DDM, the original specular bin solved using WGS 84 model is shown as a red 'X' while the new specular bin solved using DTU10 is shown with a red square. Visually, it is clear the specular bin location calculated with DTU10 is at the correct location in the reflected waveform. Range errors introduced by incorrect specular point prediction primarily impact the L1 calibration due to misidentifying the correct specular point bins (and specular region reflected power) in the DDM measurements. These errors will also degrade the surface vertical ranging accuracy and horizontal geolocation if not corrected.

B. Specular Point Solver Implementation

The new specular point solution is reported in the CYGNSS Level 1 data in the form of the specular point position and velocity variables. It takes approximately 20 seconds to calculate one day of precise specular points within CYGNSS DDMs from one satellite (approximately 320000 DDMs). The new algorithm used to solve for the specular point is as follows:

1) The original specular point solution based on the WGS84 ellipsoid model is used as our initial estimate of the specular point.

2) A large 3-D grid of points is constructed around the estimated specular point. This grid has uniform latitude and longitude spacing and is conformal to the WGS84 ellipsoid at each point.

3) At each grid point, the DTU10 mean sea surface height is used to shift the altitude. The 1-degree resolution DTU10 data (shown above) is bi-linearly interpolated to find the altitude value at each grid point. The resulting grid is then conformal to the DTU10 surface

4) Next, the point in the grid with the minimum reflection path length (from transmitter to the grid point to the receiver) is found. This minimum-path-delay grid point becomes the new specular point location estimate.

5) An additional higher resolution grid is constructed around this estimated specular point location and steps 2-4 are repeated several times. In this way, a series of search grids sequentially zoom in on the estimated specular point. The choice of initial grid size and resolution are carefully chosen to prevent erroneous convergence.
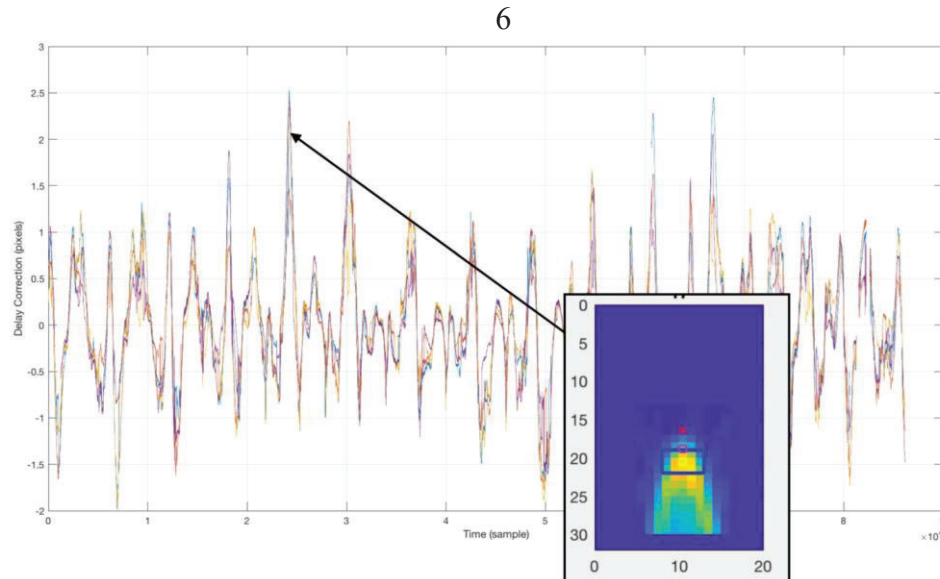

Fig. 2. One day of specular point corrections using the DTU10 model as compared to the WGS84 model. The correction due to the improved specular point solver varies between -2 and 2.5 pixels in delay space in the DDM.

The specular point we solve for here is defined as the point on the Earth with the minimum reflection path delay. As the surface we use is conformal to an arbitrary geoid topology at each grid point, no mathematical constraint is placed on transmitter and receiver incidence angles in this solution. In a strict sense, it is no longer a "specular" point since (if the ocean surface were smooth) a specular reflection would occur at surface locations with equal transmitter and receiver incidence angles, not minimum delay. Nonetheless, the minimum delay point is sufficiently relevant for our purposes since the corresponding specular bin defines the leading edge of the reflected waveform and the specular point represents the center of our iso-delay surface contours within the reflection glistening zone.

The DTU10 mean surface height model contains data over both ocean and land. The updated specular point estimates are valid and accurate over ocean only, as the DTU10 elevation model does not consider variations in land topography. An additional surface height map will be implemented in future versions of the L1 calibration which includes land surface height variations.

The updated specular point solution is differenced with the instrument estimated specular point solution to produce a correction term in the DDM's delay and Doppler space. This correction is applied to the original prediction of the specular bin location in the DDM during the estimation of the DDMA measurement area, as described in Section V(D).

IV. LEVEL 1B CALIBRATION ALGORITHM: WATTS TO SIGMA0

The Level 1a calibrated DDM represents the received surface signal power in Watts binned over a range of time delays and Doppler frequencies. Before any geophysical parameters can be estimated these power values must be corrected for non-surface related terms by inverting the forward model shown in Equation 2. The CYGNSS Level 1b calibration generates three data products associated with each Level 1a DDM: 1) A bin by bin calculation of the surface bi-static scattering cross section, σ (not normalized by scattering area), 2) a bin by bin values of the effective scattering areas and 3) a NBRCS value for a DDM Area (DDMA) in a 3 delay x 5 Doppler bin region around the estimated specular point location in the DDM. The first two products will allow users to normalize values of σ to values to σ^0 (scattering cross section per meter squared), over configurable surface extents using summations of the effective scattering areas for individual DDM bins. The values of σ are corrected for the effects of the transmit and receive antennas, range losses and other non-surface related parameters. The effective scattering areas are calculated based on the measurement specific reflection geometry and include the GPS specific delay and Doppler spreading functions. However, care should be taken when using DDM bins away from the specular point, as some of the corrections applied (such as the receive antenna gain and path losses) will degrade at pixels outside the DDMA area. An overview of the CYGNSS Level 1b Calibration is shown in Figure 3.

A. Expression For Bi-static Radar Cross Section

The final expression for the Level 1b DDM can be derived from the expression of the signal forward model, expressed in Equation 2, by solving for the scattering cross section term, $\sigma0$. As the DDM Level 1b sigma product will not be

Level 1B Calibration Summary: Power to Sigma0
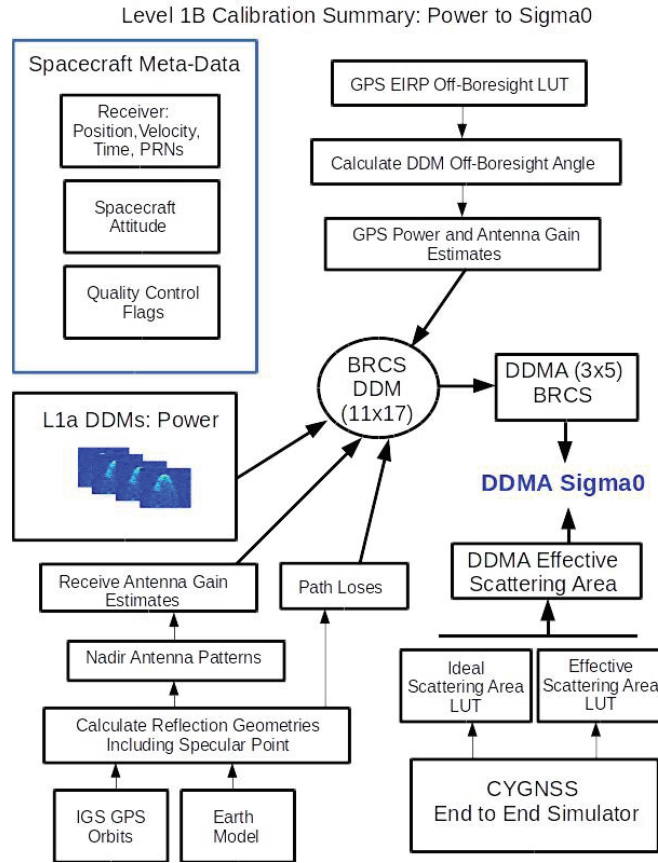

Fig. 3.Overview of CYGNSS Level 1b Calibration.

normalized, we have removed A^- from Equation 2 and replaced the normalized radar cross section σ^0 with a the non normalized, σ. Additionally, Receive antenan gain G^R_{SP}, the GPS antenna gain G^T_{SP}, and total path loss (simplified into a single value) R_{SP}^{Total} terms are approximated with their values at the specular point and applied across the whole DDM. The resulting expression for the bin by bin scattering cross section, σ, is,

$$P_{\hat{\tau},\hat{f}}^{L1b} = <\sigma_{\hat{\tau},\hat{f}}> = \frac{P_{\hat{\tau},\hat{f}}^{g}(4\pi)^3}{P^T \lambda^2 G^T_{SP} G^R_{SP} R_{SP}^{Total}}$$

(4)

where the individual terms in Equation 4 are as follows,

1) $P_{\hat{\tau},\hat{f}}^{g}$ is the Level 1a calibrated signal power at a specific delay ($\hat{\tau}$) and Doppler ($\hat{f}$) bin.

2) R_{SP}^{Total} is the total range loss from the transmitter to the surface and the surface to the receiver at the specular point. When using a relatively small area of of the DDM near the specular reflection point, this value can be approximated as the total range from the transmitter to the specular point to the receiver. This term is included in the denominator as it is calculated as a loss $R^{Total} = 1/(R^R)^2 * 1/(R^T)^2$

.

3) P^T and G^T_{SP} are the GPS satellite transmit power and antenna gain at the specular point. These values are estimated using a ground based GPS Power Monitor and measurements from the CYGNSS navigation antenna to map the transmit power of individual GPS satellites. Details can be found in [6].

4) G^R_{SP} is the receiver antenna gain at the specular point applied across all DDM bins. The SP antenna gain outside the DDMA region will introduce errors that should be accounted for when using pixels outside the DDMA region (3 delay and 5 Doppler around SP).
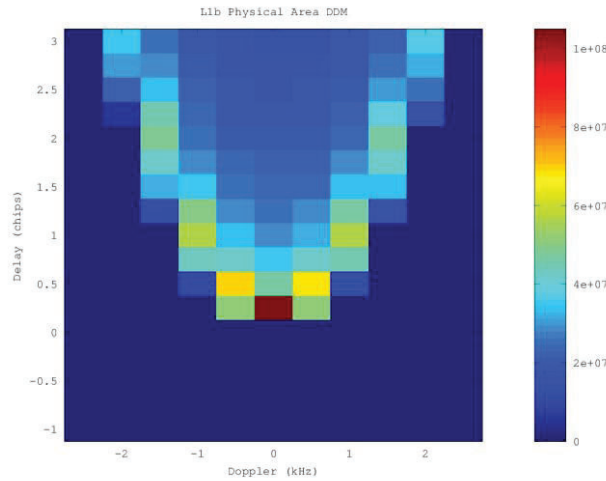
8

Fig. 4. Physical Scattering Area for a typical DDM reflection geometry. The delays before the specular reflection point do not correspond to any physical region on the surface.

B. Calculating Effective and Physical Scattering Areas

A single delay Doppler bin will contain the captured scattered power across one or more physical regions on the ocean surface. For each delay Doppler bin in the DDM this region will vary both in actual physical size (on the ground surface area) and effective area (combined with the GPS spreading functions). The GPS ambiguity functions (in both delay and Doppler) increase the effective area of each delay Doppler bin, causing power to be "spread" into adjacent delay and Doppler bins from outside the geometry determined physical scattering area. These functions change the levels of overall processed power observed. The physical area of each DDM bin can be calculated as follows,

$$A_{\hat{\tau},\hat{f}} = \iint_A dxdy$$

(5)

An example of the physical scattering are for a typical DDM is shown in Figure 4. Note that points up to and before the specular point bin (i.e. at delays shorter than the specular reflection point delay) have no physical surface scattering area. The power received in the bins before the specular point is due to

power being spread into these bins by the GPS ambiguity functions from physical areas near the specular point. The effective surface scattering area for each delay/Doppler bin is expressed as the ambiguity function weighted surface integration,

$$\bar{A}_{\hat{\tau},\hat{f}} = \iint\limits_{A} \Lambda^2_{\hat{\tau};x,y} S^2_{\hat{f};x,y} dxdy$$

(6)

where the delay spreading function, $\Lambda_{\hat{\tau};x,y}$ and the Doppler spreading function, $S_{\hat{f};x,y}$, are integrated over the physical surface corresponding to each individual delay/Doppler bin. Figure 5 shows the effective scattering area DDM corresponding to the physical scattering areas illustrated in Figure 4.

Initial analysis has shown that when only using a relatively small area of the DDM (corresponding to approximately a $25km^2$ area on the surface), it is sufficient to approximate the receive antenna gain, range loss terms and the GPS transmit antenna power and gain using constant values calculated at the specular reflection point.

C. On-Orbit Estimation and Correction of Receive Antenna Pattern Errors

As a standard Level 1 data product, CYGNSS data include DDMs over 11 Doppler bins $\hat{f}$ and 17 delay ($\hat{\tau}$) pixels around the specular point. The NBRCS $\sigma_{\hat{\tau},\hat{f}}$ is calculated as per Equation 4 for each delay/Doppler bin.

Prior to launch, antenna pattern measurements were made for all of the port and starboard antennas. In addition, the predicted effects of the spacecraft body where extensively modeled using pattern simulation tools to attempt to accurately predict the final antenna patterns when attached to the spacecraft. These simulations included mechanical CAD models of the physical spacecraft with electromagnetic field simulations using the FEKO and Savant software packages. and input
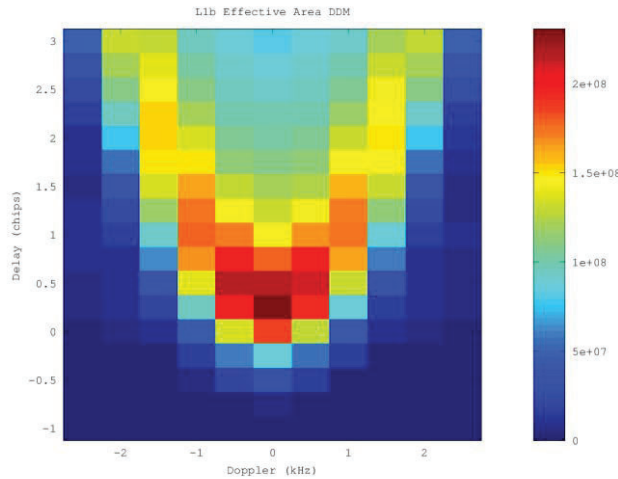
9

L1b Effective Area DDM

Fig. 5. Effective scattering area corresponding to the physical scattering area shown in Figure 4. This DDM of effective scattering area is a key output product of the Level 1b calibration which allows users to calculate normalized values of σ^0.

into Additionally, full pattern measurements of the port and starboard antennas were made while mounted to a CYGNSS Engineering Model (EM) in an anechoic chamber. From the modeling effort, which was confirmed by the EM chamber measurements, we know that the solar panels have a significant impact on the observatory antenna gain patterns.

The individual modeled pattern measurements were adjusted using a constant gain factor based on measured differences between the flight antennas to create the at-launch gain patterns for each CYGNSS flight model (FM) antenna calibration tables.

However, we know that there is potentially significant variability in the exact deployed positions of the solar panels from repeated pre-launch panel deployment tests. It therefore stands to reason that applying a simple constant offset for each of the FM antennas from the modeling and EM measurements is overly simplistic. It was evident from the initial analysis of the CYGNSS on-orbit data that an improved estimate of the CYGNSS antenna patterns was needed for each antenna in the constellation.

1) Estimation of Receive Antenna Gain Error: Analysis of the initial CYGNSS data, released in May of 2017, show a significant dependence of observed σ_0 on the azimuthal observation angle of the specular point with respect to the CYGNSS spacecraft. While the NBRCS values are expected to depend on wind and on incidence angle, the dependence on azimuthal angle was expected to be negligible. These anomalies were quantified in terms of a normalized NBRCS anomaly ($\sigma_{0,anom}$), expressed as:

$$\sigma_{0,anom} = \frac{(\sigma_0 - <\sigma_0>)}{<\sigma_0>}$$

(7)

σ_0 is expected to vary as a function of wind speed and geometry, so σ_0 anomalies are computed as the difference between each calibrated σ_0 from the mean value for all σ_0 within 2 meters per second wind speed and 2 degree incidence angle bins. Reference wind speeds are from collocated ECMWF reanalysis fields to within 90 minutes and 25 kilometers of the corresponding CYGNSS observations. To determine the dependence of these anomalies on azimuth angle, average anomalies were computed in 1 degree azimuth bins. The results using the original calibration algorithm between day of year 77 and 121 are shown in Figure 6. Results are averaged across all 8 CYGNSS satellites for the starboard and port antennas. For this and future analysis shown, the average of the σ_0 in the DDM is computed using the estimates *sigma*$_0$ over the DDMA region near specular point DDM bins. It is important to note that due to the cross track ground projection of the receive antenna patterns and on-board track selection algorithm, most of the measurements are distributed within 30 degrees in azimuth angle around 90 degrees (for the Starboard) and 270 degrees (for the Port) measurement orientations.

The key variables in the Level 1b calibration are the transmit power P^T, transmit antenna gain G_{SP}^T, the receiver antenna gain G^R, and geometric factors including the range correction R_{SP}^{Total}. Additionally, the effective scattering area used to normalizing σ also contributes to the overall level of σ_0. Of these, only the antenna gain patterns G^T and G^R depend directly on azimuthal angle. The transmit antenna gain G^T will vary from observation to observation, but not in a manner highly correlated with specular point azimuth with respect to the CYGNSS spacecraft. Therefore, it was hypothesized that the likely candidate for the observed azimuthal variation was the receiver antenna gain G^R.

2) Improved CYGNSS Antenna Patterns: On-orbit estimates of $\sigma_{0,anom}$ described above have been calculated for all CYGNSS flight antennas. For each flight antenna in the constellation (1 port and 1 starboard antennas for each of 8 spacecraft = 16 total antennas), $\sigma_{0,anom}$ anomalies were computed in 1 degree increments of spacecraft off-nadir and azimuth angle. These antenna correction maps were then smoothed over 5 degree windows in azimuth and off-nadir angle in order to reduce measurement noise.

These results were then interpolated using nearest neighbor interpolation to a resolution of 0.1 degree. This map of $\sigma_{0,anom}$ as a function of antenna coordinates was used to scale the original patterns to produce a new estimate of the receive pattern gain, which greatly reduced the observed azimuthal anomalies (anomaly subtracted from original antenna pattern in logarithmic space from estimates of gain in dB). This was done for all 16 operational flight antennas on all 8 observatories.

The resulting $\sigma_{0,anom}$ anomalies gain maps as a function of azimuth averaged across all 8 spacecraft is shown in Figure 6. The anomalies, which were initially greater than as 40% are reduced to less than 20% residual anomalies across all azimuth angles. The regions near the azimuth angles where most measurements are taken (90 and 270 degrees for Starboard and Port, respectively) have errors reduced to 10% or less. The remaining errors are most likely due to variability within the data not related to wind speed, incidence angle, or receiver antenna pattern effect accounted for in this analysis.

It should also be noted that off-nadir angle is highly correlated to incidence angle for a given spacecraft orientation, with the relationship directly tied to the spacecraft roll, which changes periodically as the spacecraft are adjusted to maintain a power positive orientation for high solar beta angles.

An example of the original pre-launch CYGNSS receive antenna gain patterns for the CYGNSS FM1 starboard antenna and gain corrections applied are shown in Figure 7.

D. Digital to Analog DDM Scaling Issue

In the original CYGNSS L1a calibration algorithm, the entire Level 1a DDM was scaled from digitally sampled DDM values to the equivalent analog sampled power based on the 2-bit analog to digital sample distribution. This correction was based on well known methods in radio astronomy for dealing with finite digital sampling of analog signals. However, examination of closely geo-located tracks between different observatories at very close time intervals revealed an observed bias between measurements over nearly identical conditions. Figure 8 (top) shows one such case, where FM6 and FM8 pass over nearly the same surface within 5 minutes of each other, yet a clear difference in the NBRCS values can be observed over the length of the track. Upon subsequent investigation, an issue in the analog to digital scaling being applied was found, in which the calculated correction between digital and analog measurements was not correct and introducing significant statistical biases between observatories.

Upon removal of the existing digital to analog scaling the overall inter-satellite bias statistics improved significantly. Figure Figure 8 (bottom) shows the same two tracks after the scaling has been removed, with good agreement across the entire track.

The exact problem with the digital to analog scaling is being investigated and has not yet been identified. However, as a significant reduction in inter-satellite measurement bias was demonstrated with the removal of the digital to analog scaling factor, it will be included in the next public data release.

E. Calculating a Normalized Bi-static Radar Cross Section

The Level 1b bin by bin DDM of σ and the bin by bin DDM of effective scattering areas can be combined to calculate a normalized radar cross section value, σ^0, over selected regions of the

measurement DDM called the DDMA. The CYGNSS Level 2 wind retrieval products use the DDMA to generate geophysical model functions (GMF) to estimate near surface winds. The DDMA consists of 3 delay bins and 5 Doppler bins, with the specular point located in the first row (shortest delay) of this region. Figure 9 shows this DDMA region in red, overlapped with the normal instrument processed DDM delay and Doppler pixels in black. The true (best estimate) of the DDMA region (as calculated by the precise specular point estimation method described above) is marked as a red dot in this figure, while the white dot is the Level 1b DDM that the "true" specular point falls in.

   These precise DDMA bins will not normally align exactly with the L1b DDM bins generated by the instrument (due to errors in the instruments open loop signal tracker) making a simple summation over 15 total bins in the L1b DDM problematic. The "true" DDMA radar cross section is the weighted combination of L1b DDM bins around the best estimate surface specular point and fractional contributions from bins around the edge of the DDMA region. This set of overlapping
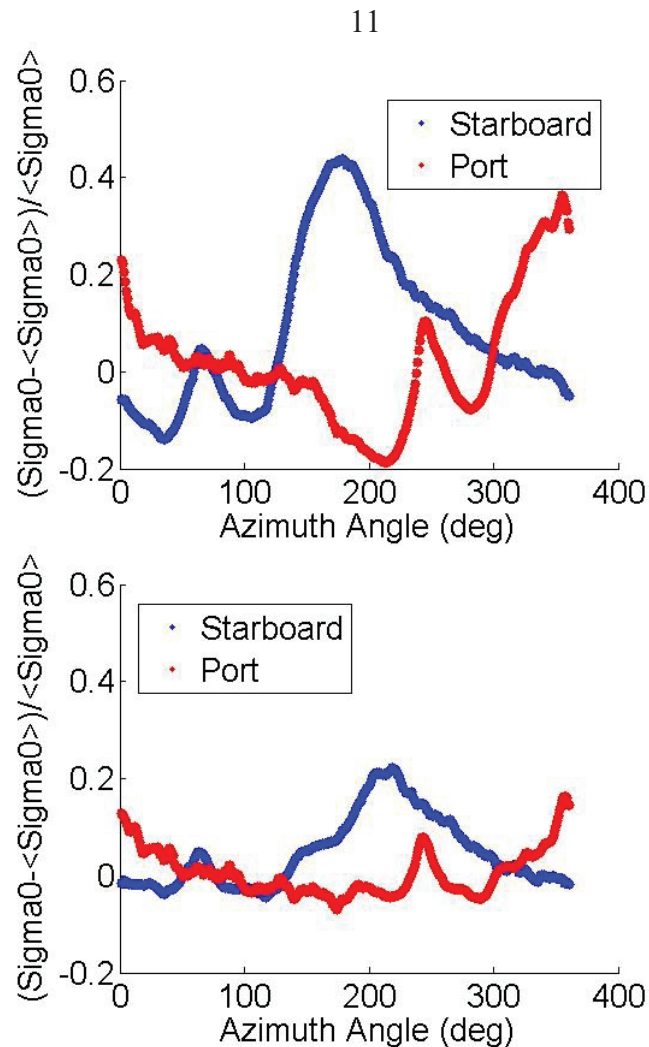

Fig. 6. (above) σ_0 anomalies computed for Level 1 data between day of year 77 and 121 of 2017 on the Version 1 using pre-launch estimated receive antenna patterns. (below) σ_0 anomalies computed for Level

1 Corrected data for Version 2 of the L1 calibration. The anomalies reduce the worst case error of 40% to less than 10%.

DDM bins is, when weighted and summed, the best estimate of the "true" multi-bin DDMA total radar scattering cross section σ_0. The mis-alignment between the measured L1b DDM bins and the "true" DDMA bins is illustrated in Figure 9. The DDMA specular point is offset by fractional bin amounts in delay (δ) and Doppler (Δ) from the L1b measurement DDM shown in the figure.

In order to calculate the total radar cross section in the red DDMA area, the actual measurement L1b values (one per white box/pixel) need to be combined using a weighting scheme that includes only a fractional amount of power from bins around the edges of the DDMA bins. The fractional weighting scheme used is approximated to be linear in both the delay and Doppler dimensions. Figure 9 shows the regions of overlap for a single red DDMa bin with respect to the surrounding measurement bin values.

The total DDMA radar cross section can be calculated as per Equation 8, resulting in a combined expression for the DDMA σ^0,

$$\sigma^0 = \frac{\sigma_{weighted}}{A_{total}} = \frac{W_{i,j} \sum_{i=1}^{N} \sum_{j=1}^{M} \sigma_{\tau_i, f_j}}{\sum_{i=1}^{N} \sum_{j=1}^{M} A_{\tau_i, f_j}}$$

(8)

where N and M represent the delay and Doppler bin in the L1b DDM, respectively (with N = 4 and M = 6, a single bin more than the DDMA size in both dimensions)
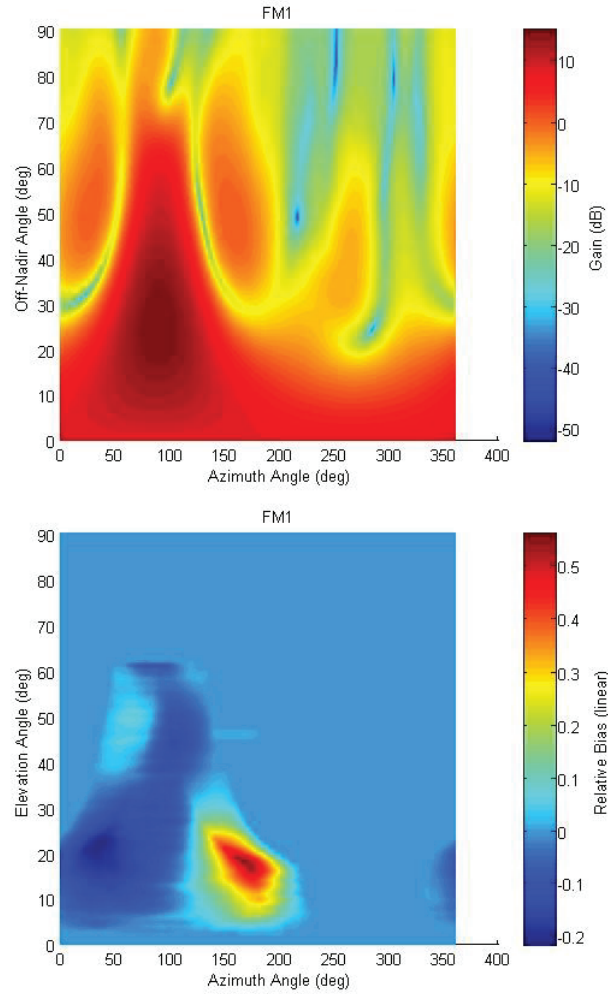
Fig. 7. (above) Original FM1 starboard antenna pattern. (below) FM1 starboard antenna pattern corrections applied to produce the improved FM1 starboard antenna pattern.

$$
\begin{aligned}
\sigma_{weighted} = \; & (1 - \delta)(1 - \Delta)\sigma_1 + (1 - \delta)(\sigma_2 + \sigma_3 + \sigma_4 + \sigma_5) \\
& + (1 - \delta)\Delta\sigma_6 + (1 - \Delta)(\sigma_7 + \sigma_{13}) + \Delta(\sigma_{12} + \sigma_{18}) \\
& + \delta(1 - \Delta)\sigma19 + \delta(\sigma20 + \sigma21 + \sigma22 + \sigma23) + \delta\Delta\sigma24 \\
& + (\sigma8 + \sigma9 + \sigma10 + \sigma11) + (\sigma14 + \sigma15 + \sigma16 + \sigma17)
\end{aligned}
\tag{9}
$$

Each bin in the L1b DDM contributing to the weighted $\sigma_{weighted}$ is scaled by a weighting factor $W_{i,j}$ based on the overlap with the respective "true" DDMA bin. $\sigma_{weighted}$ is then normalized by the sum of the effective area DDMA bins (which are centered at the ideal specular reflection point and require no weighting correction) to arrive at the final σ^0 measurement over the "true" DDMA region. The summations and weighting involved in calculating $\sigma_{weighted}$ for the example above is expressed in Equation

9, where the delay and Doppler index values are simplified to single bin numbers as illustrated in Figure 9, and terms with the same weighting factor are combined.

F. Altitude Dependant DDMA Area Normalization

The CYGNSS satellites where launched into slightly elliptical orbits, causing altitude fluctuations between perigee and apogee of up to approximately 35 km. This was not taken into account in the V2.0 calibration algorithm, where a circular orbit at a constant altitude was assumed during the generation of the initial look-up-tables (LUTs) used to perform the
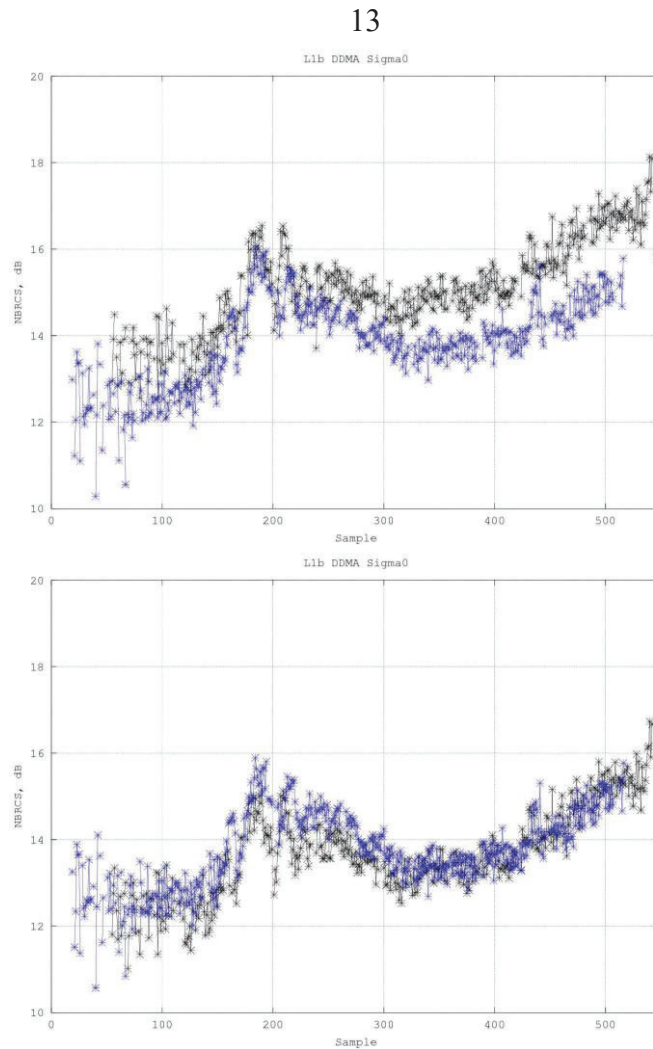
13

Fig. 8. (top) Inter-satellite bias between tracks of FM6 and FM8 on August 23rd less than 5 minutes apart. (bottom) After digital to analog scaling removed NBRCS values agree much better across the same ocean track.
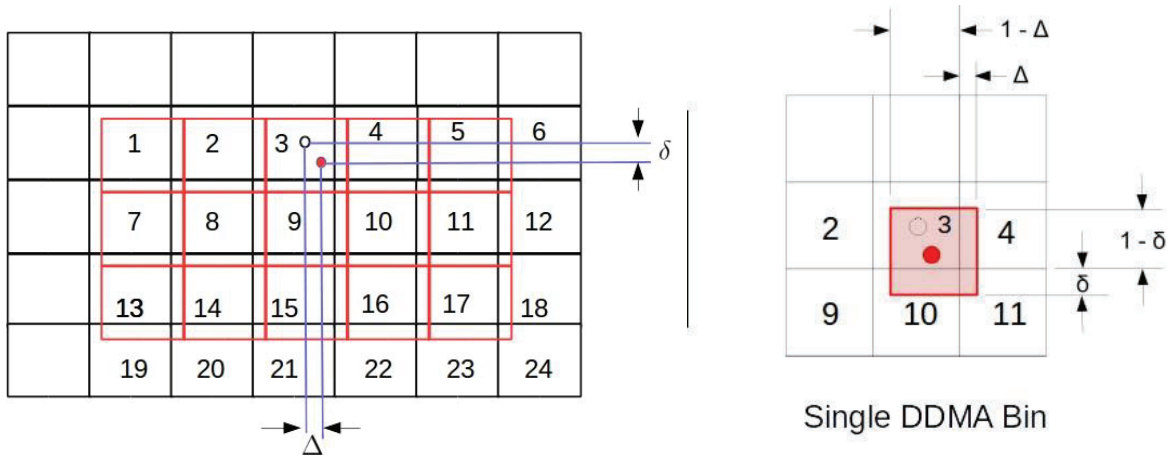
Fig. 9. (left) Level 1b DDM of σ values. Numbered to correspond to same pixels with DDMA overlayed and bin numbers referenced to Equation 9. The red group of DDMA bins is the overlay of the 3 by 5 DDMA measurement area with the processed Level 0 DDM pixels, containing a typical mis-alignment. The best estimate DDMA, is based on a refined specular point estimate and represents the true measurement error. (right) Detail of the overlap areas of a single DDMA bin (the specular point bin) and adjacent L1b bins.
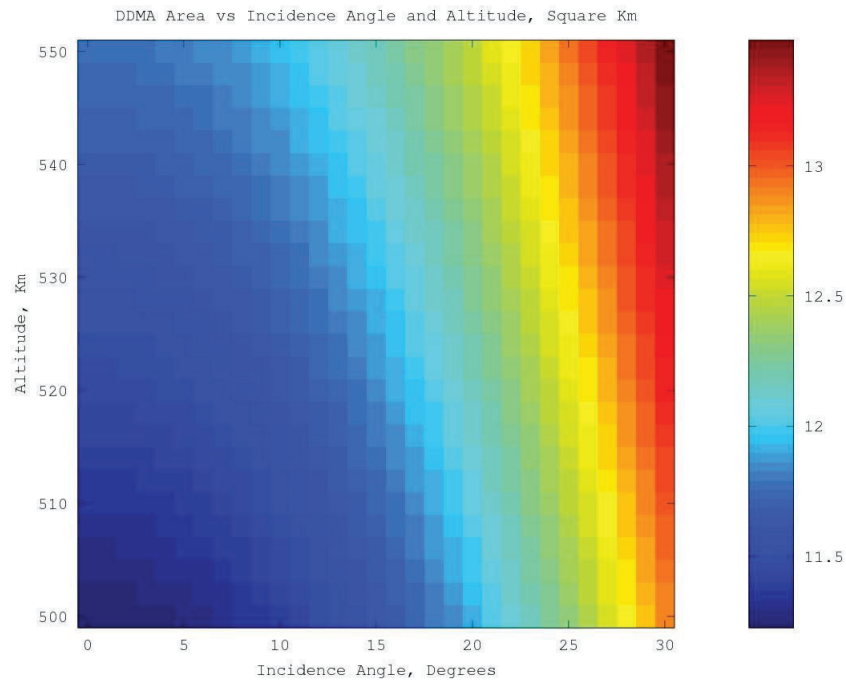
14

Fig. 10. Version 2.1 DDMA Area LUT values for altitudes between 500 and 550 km (covering the full range of the CYGNSS orbits, with margin on the low side), and incidence angles between 0 and 30 degrees. The increases in DDMA area with incidence angle and altitude are both clearly observable in

the new LUTs. These data were generated at a constant 90deg azimuth angle. Color scale is in square kilometers for the entire DDMA region.

scattering area normalization of the DDMA, to arrive at NBRCS estimates of σ_0. This has been corrected in Version 2.1 with an updated normalization area LUT which accounts for the changing altitude of the CYGNSS spacecraft.

After the calculation of the weighted DDMA sigma total as described above, $\sigma_{weighted}$, the bistatic scattering cross section is normalized as shown in Equation 8. In the Version 2.0 version of the calibration this was performed with a look-up-table which was a function of incidence angle and elevation angle only, at a constant altitude. This ignored the effects of the changing satellite altitudes and introduced (relatively) small errors (up to 0.1 dB) into the σ_0 estimation used in subsequent wind speed and MSS retrievals. In Version 2.1, a new LUT has been generated with an additional altitude dimension. This will allow the area normalization to correct for changes in the scattering area due to their slight eccentricity, as well as longer time scale orbit changes. An example sub-set of the new DDMA normalization areas (reduced to better reveal the changing LUT area magnitudes) is shown in Figure 10 as a function of incidence and altitude (at a constant azimuth angle). Testing of the new altitude dependent LUT has been validated to significantly reduce correlation of σ_0 with the satellite altitude.

G. Correction for Dependence of Calibration Error on Receiver Noise Floor

The v2.0 L1b calibration algorithm produces two measurement observables, DDMA and LES, which are subsequently used by the L2 algorithm to retrieve wind speed. The correction described here is added to the v2.1 L1b calibration algorithm. It applies a small additive offset to each observable. The correction minimizes mean differences between the measured observable and simulated values of the observable obtained by applying the geophysical model function to coincident wind speeds modeled by ECMWF. The correction is a linear function of the noise floor of the DDM from which the observable is computed. The slope and y-intercept of the linear function are themselves functions of the Flight Model (FM) number, the Range Corrected Gain (RCG), and the angle of incidence (θ_{inc}) associated with each DDM. The correction applied to each L1 observable has the form,

$$Obs_{corr} = Obs + m(FM,RCG,\theta_{inc})NF + b(FM,RCG,\theta_{inc}) \tag{10}$$

where,

- Obs_{corr} is the corrected L1 observable.
- Obs is the v2.0 L1 observable, either the DDMA (σ_0) or the LES.
- $m(FM,RCG,\theta_{inc})$ is the slope of the linear regression, which is a tabulated function of FM, RCG and θ_{inc}.
- NF is noise floor of the DDM (designated as ddm noise floor in the L1 data files).
- $b(FM,RCG,\theta_{inc})$ is the y-intercept of the linear regression, which is a tabulated function of FM, RCG and θ_{inc}.

H. Characterization of GPS Effective Isotropic Radiated Power (EIRP)

The GPS Transmit Power, P_T and transmit antenna gain, G_T, or the effective isotropic radiated power (EIRP) can be estimated using a combination of ground based measurements and a parametrized model as a function of the transmitter space vehicle (SV) for all GPS satellites.

Transmit Power Estimation

A ground-based GPS constellation power monitor (GCPM) system has been designed, built, calibrated, and operated to measure the direct GPS L1 C/A signal [6]. The calibration subsystem and low noise amplifier (LNA) are implemented on a PID controlled thermal plate with extremely stable temperature control.

The measured GPS received power has been found to be highly repeatable, as tested for different satellites of three different block types. The measured EIRPs are verified by DLR/GSOCs independent measurements using a calibrated 30 m dish antenna with 50 dB L-band gain.

An optimization algorithm is used to estimate the transmit power of GPS L1 C/A-code by minimizing a cost function based on the difference between an engineering forward model prediction and the measurement of received power. We determine our best estimate of the GPS transmit power for L1 C/A signal by averaging 32 days of estimates of P_T, as given in Table I. More technical details of the GCPM system and the optimization algorithm can be found in [6].

PRN	P_T (dBW)	Block	PRN	P_T (dBW)	Block
1	15.09	IIF	17	16.39	IIR-M
2	13.79	IIR	18	14.04	IIR
3	14.77	IIF	19	13.66	IIR
4	-	-	20	13.48	IIR
5	16.28	IIR-M	21	14.43	IIR
6	15.38	IIF	22	14.39	IIR
7	16.86	IIR-M	23	15.41	IIR
8	15.42	IIF	24	15.03	IIF
9	15.49	IIF	25	15.32	IIF
10	16.28	IIF	26	15.22	IIF
11	13.67	IIR	27	15.34	IIF
12	16.88	IIR-M	28	14.27	IIR
13	13.89	IIR	29	16.84	IIR-M
14	13.20	IIR	30	15.47	IIF
15	16.08	IIR-M	31	16.35	IIR-M
16	13.93	IIR	32	15.87	IIF

TABLE I. Estimates of GPS Transmit Power (Level 1 C/A) for v2.1.

It should be noted that:

1) The estimated power values are indeed an "effective transmit power", as the product of the exact transmit power and the transmit system gain correction factor (GCF).
2) The accuracy of the estimated power values are dependent on the accuracy of the baseline pattern (5th order power series of transmit antenna gain in [7]) used in the forward model simulation.

Transmit Antenna Gain Estimation

The transmit antenna directivity of IIR and IIR-M block type SVs has been published in [7], while that of IIF block type
SVs is unavailable to public. The baseline antenna pattern [8] used in the Level 1 calibration is a 5th order power series (polynomial fitting) of the azimuthally averaged published antenna pattern for IIR and IIR block and that of the averaged pattern of all 12 SVs using improved antenna panel (4 IIR and 8 IIR-M) for IIF block.

Discussion on GPS Transmitter EIRP Characterization

1) Transmit power and antenna pattern: The high resolution full transmit antenna pattern will be retrieved using the direct GPS signal measured by the CYGNSS zenith antenna, as discussed in [9]. Then the transmit power table will be further updated when the full patterns are applied to the optimization algorithm.

2) IIF block type power switching issue: 10 of the 12 IIF SVs switch the power sharing between the components in L1 over US east-coast and back over west-pacific in every orbit. It has been a stable behavior since the first quarter of 2017. Currently, the data measured by IIF block is flagged. This issue will be resolved by incorporating the CYGNSS zenith antenna measurement in Level 1 calibration.

3) SV retirement for PRN 18: On March 5th, 2018, SVN 54 (operating as PRN 18) retired. SVN 34 (Block IIA) is used for PRN 18 since March 20th, 2018. CYGNSS data using PRN 18 since then is flagged.

4) Power redistribution for block IIR-M: A commanded redistribution of transmit power from M-code to C/A-code was performed for the 7 active IIR-M satellites on February 7 and February 8, 2017 [10]. The measured carrier-to-noise (C/N0) density ratio from different geodetic receivers experienced an approximately 1.5 dB-Hz increase on average. This phenomenon indicates an increase in the L1 C/A-code power for all 7 satellites after the maintenance was performed [11]. This event happened before the CYGNSS satellites were transitioned to science mode. No additional power redistribution for IIR-M satellites is reported since then.

V. Zenith EIRP Calibration (v3.0 calibration)
Summary of Changes from v2.1 Approach

The v2.1 L1 calibration algorithm assumes a static value for the GPS transmit power and determines the GPS transmit antenna gain in the direction of the specular reflection point using an off-boresight azimuthal averaged estimate of the individual GPS transmitters. The GPS transmiter off-boresight antenna gains in the v2.1 CYGNSS calibration are based on publicly available pre-launch measured patterns provided by Lockheed-Martin. Additionally, release-controlled pre-launch pattern estimates for the Boeing Block IIF satellites were obtained and used to generate off-boresight gain look up tables for the GPS IIF satellites. For GPS transmitters with out pre-launch patterns, an approximate pattern was estimated using the best available information.

Generally, these simplified one-dimensional GPS transmit antenna pattern approximations worked well enough to meet the low wind speed requirements. However, it suffers from a number of known problems which are addressed with the next version (v3.0) of the CYGNSS calibration algorithm, including,

1) The on-orbit GPS transmiter antenna patterns are known to contain differences from the pre-launch measured patterns, as the pre-launch measurements were not made while attached to the flight spacecraft bus. This most likely resulted in pattern distortions as the antenna interacted with the spacecraft and additional avionics present on the same face as the GPS transmit antenna, which were not considered when the pre-launch measurements were made.

2) It is generally understood that multiple GPS transmitters (notable the entire Block IIF satellites) operate using flexible transmit power levels. This occurs when the GPS operations center, without any announcement, will change the transmit power level of a GPS satellite for various but unknown reasons. This results in un-predictable jumps in the transmit power which are not accounted for in the v2.1 calibration algorithm, which assumes a constant transmit power level. These "flex-power" variations on the IIF block satellites necessitated the flagging out of all measurements from IIF satellite, greatly reducing the CYGNSS measurement coverage.

The v3.0 calibration algorithm is designed to greatly mitigate the above two error sources by estimating the GPS transmit power and antenna gain (Effective Isotropic Radiated Power, EIRP) using measurements from the direct (zenith) navigation channel of the CYGNSS delay Doppler mapping receiver (DDMI). By directly monitoring and linking the calibration to the direct observation of the GPS transmitter, the unpredictable flex-power changes can be detected instantly. Additionally, the new calibration technique requires only a ratio of the differences of the GPS EIRP between the direct and reflected instrument channels, resulting in lower uncertainties in the azimuthal asymmetries of the GPS transmit antenna patterns.

The (v3.0) Zenith EIRP Level 1 Calibration algorithm uses the same Level 1 calibration equation to calculate the delay Doppler Map bistatic radar cross section values (repeated below).

$$\bar{\sigma}(\hat{\tau}, \hat{f}) = \frac{P_g(\hat{\tau}, \hat{f})(4\pi)^3}{E'_S \lambda^2 G_S^R R_S^{Total}}$$

(11)

where, the two GPS transmitter terms are combined into a single term expressing the effective Isotropic Radiated Power (EIRP), consisting of the GPS transmitter power level and the GPS transmitter antenna gain in the direction of the specular point (SP), corrected by the ratio of receiver LNA gains. The combined GPS transmitter EIRP is expressed as,

$$E'_S = P_S^T G_S^T$$

(12)

The essential difference in the v3.0 calibration algorithm is that the GPS transmitter EIRP is estimated in real time using observations from the CYGNSS zenith navigation antenna, as opposed to using fixed look up table entries. The Zenith EIRP estimation used in the v3.0 calibration is described below.

Estimating the specular GPS EIRP using Zenith Navigation Signals

Estimating the GPS transmitter EIRP in the direction of the CYGNSS zenith antenna starts with the Friis equation for the received GPS power at the receiver,

$$P_Z = \frac{E_Z \lambda^2 G_Z}{(4\pi)^2 R_Z^2}$$

(13)

where, E_Z is the GPS transmitter EIRP toward the zenith CYGNSS antenna, G_Z is the CYGNSS zenith antenna gain, R_Z is the path distance from the GPS transmitter to the CYGNSS satellite. This expression can be rearranged to an expression for the GPS zenith EIRP (E_Z),

$$E_Z = \frac{(4\pi)^2 P_Z}{G_Z \lambda^2 L_Z}$$

(14)

Each of the terms in Equation 14 are calculated as,

- G_Z is estimated using the derived CYGNSS zenith antenna gain pattern over the full upper hemisphere of observation angles.

- L_Z is the range loss, calculated from the signal path as $L_Z = \frac{1}{R_Z^2}$, using the estimated CYGNSS receiver position (from its on-board navigation solution) and the GPS satellite position from the published IGS GPS ephemeris.

- P_Z is the estimated EIRP signal power at the CYGNSS receiver.

The raw power measurement of the zenith signal, $C_Z = I^2 + Q^2$ (in units of counts), is related to the signal power referenced to the input to the DMR by,

$$P_Z = 10^{0.1(a(C_Z,dB)^2 + b(C_Z,dB) + c)}$$

(15)

where $C\_Z, dB = 10\log_{10}(C\_Z)$. The scaling quadratic regression coefficients (a,b,c) are derived from laboratory characterization tests of the EMulator, and P_z is in units of Watts. The default v3.0 zenith power conversion coefficients are shown in Table 1 below.

Coefficient	Value
a	0.011897122540965
b	-0.509944684931564

c	-1.511603333176575e+02

Table 1, Zenith counts to power conversion coefficients

Subsequently, the EIRP of the GPS transmit signal in the direction of the CYGNSS specular point (E_S) can be related to the GPS EIRP in the direction of the zenith antenna (E_Z) with two correction terms: a) the ratio of the analog LNA hardware gains between the two channels and b) a correction for the slightly different line of sight between the zenith and specular point directions. To facilitate this, new expressions for E_S and E_Z can be used which include their respective LNA analog gains, such that,

$$E'_s = E_s A_s \tag{16}$$
$$E'_z = E_z A_z \tag{17}$$

In practice, the GPS EIRP towards the specular point can be calculated as a function of the LNA analog gain ratio and the ratio of the GPS EIRP values due to slightly different viewing geometry. Resulting in the following expression for the GPS EIRP towards the specular point,

$$E'_S = E'_Z \frac{A_S}{A_Z} \frac{E_S}{E_Z} = E'_Z [SZR_A][SZR_E] \tag{18}$$

Where,

- A_s/A_z is the ratio of the specular channel LNA analog gain and the zenith channel analog gain. Which is a function of CYGNSS FM and the specular (T_s) and zenith (T_z) LNA temperatures, respectively.

- E_s/E_z is the ratio of the specular channel GPS EIRP and the zenith channel EIRP, and is a function of the GPS transmitting Space Vehicle (SV) and the specular reflection incidence angle (theta).

- The SZR_A is the Specular to Zenith Ratio expression for A_s/A_z , which is a function of the CYGNSS observatory FM and LNA temperatures.

-The SZR_E is the Specular to Zenith Ratio for E_s/E_z, which is a function of the GPS transmitter and specular point incidence angle.

The specular-to-zenith EIRP ratio (SZR_E) is the azimuthally integrated ratio of the GPS transmit antenna gain in the direction of the zenith antenna to the gain in the direction of the specular reflection point, expressed as,

$$SZR_E(SV, \theta) = \int_0^{2\pi} \frac{G_Z^T(SV, \theta, \phi)}{G_S^T(SV, \theta, \phi)} d\phi \tag{19}$$

where phi is the azimuth coordinate of the GPS antenna gain pattern. The SZR ratio is a function of GPS SV number and of the incidence angle (theta) of the specular reflection point.

The ZSR_A is determined using the pre-launch characterized LNA gain vs temperature look-up-tables. The ZSR_E is estimated with empirically determined GPS transmitter antenna patterns, and converted to a look-up-table as a function of the specular point incidence angle for all GPS transmitters as a function of their SV number. For each measurement, the PRN number is converted to SV number from the latest available mapping of SV to PRN.

Finally, the estimated value of E'$_S$ is substituted into the L1b calibration equation 1 and used to generate the v3.0 L1b BRCS DDM.

Rescaling of Nadir Antenna Patterns

Version 2.1 of the CYGNSS data includes a rescaling of the at-launch assumed zenith antenna patterns based on matchups of CYGNSS derived L2 winds with model-based matchups. These L2 estimates are based on empirically derived geophysical model functions connecting L1 normalized bi-static radar cross-section (NBRCS) estimates that are themselves based upon the antenna patterns and model-based matchups themselves. In order to place the antenna pattern rescaling on a more physically sound basis, the Version 3 antenna patterns were rescaled using matchups with model-based estimates of MSS.

The relationship between MSS as a function of incidence angle θ is given by:

$$\text{NBRCS}(\theta) = \frac{|R|^2}{MSS} \tag{20}$$

Where R is the Fresnel coefficient evaluated at θ. For the version 3 antenna pattern rescaling, match-ups between IFREMER WaveWatch III (WW3) estimates of MSS and CYGNSS data were created for all data in 2019 with the CYGNSS data filtered by the overall Level 1 quality control flag. In order to match the wave spectra of CYGNSS derived MSS, the tail of the IFREMER MSS spectra were extended assuming an Elfouhaily wave spectrum. With this extended WW3 MSS, a model based NBRCS was computed using Equation 20. For each CYGNSS, WW3 MSS matchup, the mean ratio of the observed to model NBRCS was computed in 1 degree bins of antenna elevation and azimuth angle for all 16 CYGNSS nadir antennas (port and starboard antennas of all 8 satellites) within a range modelled NBRCS of 30-40, which contains 20% of the observed data while focusing on the peak of the NBRCS distribution (Figure 11). The distribution of the ratio of observed to model NBRCS for 2019 data is shown in Figure 12. This ratio has mode of 0.5, leading to a resulting rescaling of the antenna patterns of around 3 dB (e.g., Figure 13). A comparison of model and retrieved NBRCS before and after rescaling is shown in Figure 14. A comparison of the model and CYGNSS MSS after rescaling is shown in Figure 15. In addition to producing MSS estimates that agree much more with model estimates, the antenna pattern rescaling also results in NBRCS estimates that vary less from antenna to antenna as shown in Figure 16.
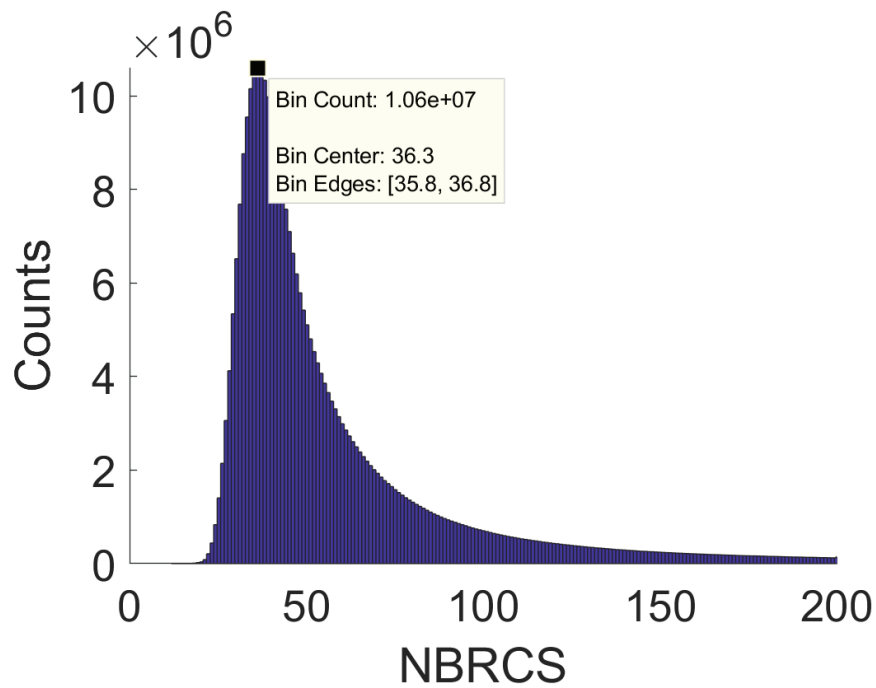
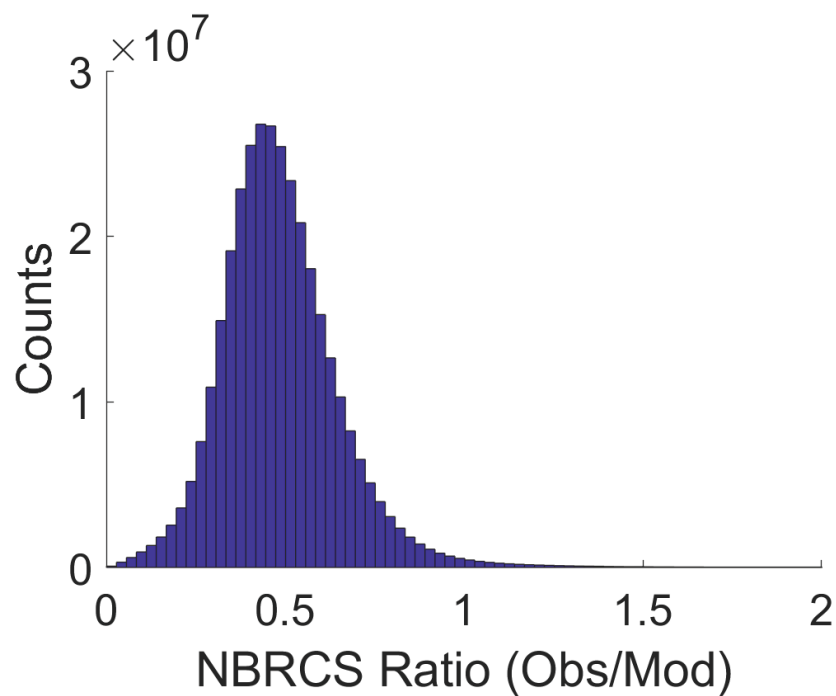Figure 11. Distribution of model based NBRCS from WW3 data for 2019.

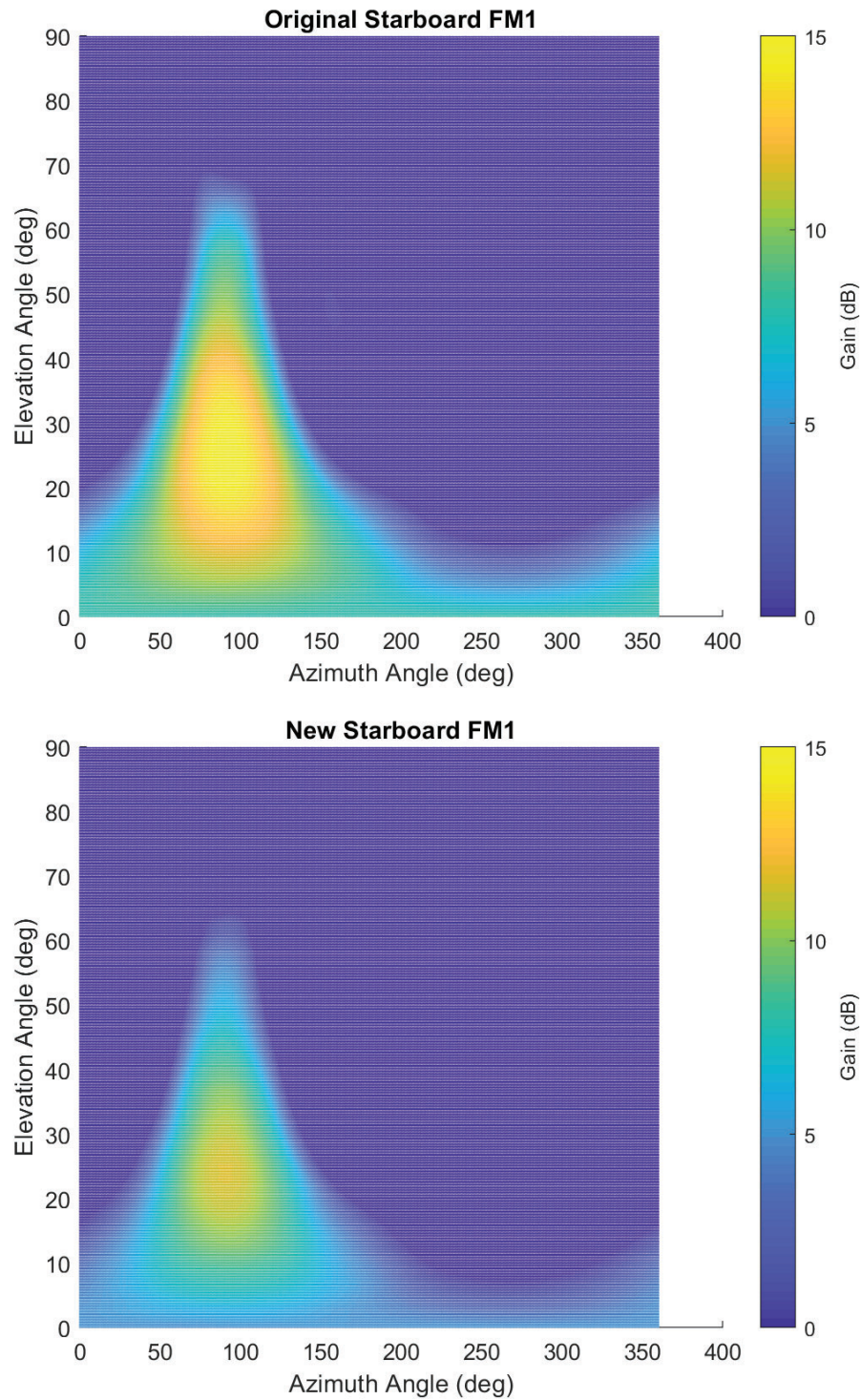Figure 12. Distribution of ratio of observed to model based NBRCS for 2019 data.

Figure 13. Original (top) and updated (bottom) antenna patterns for CYGNSS satellite 1 starboard antenna. Other antenna pattern rescaling are similar. Peak gains were reduced by about 3 dB.
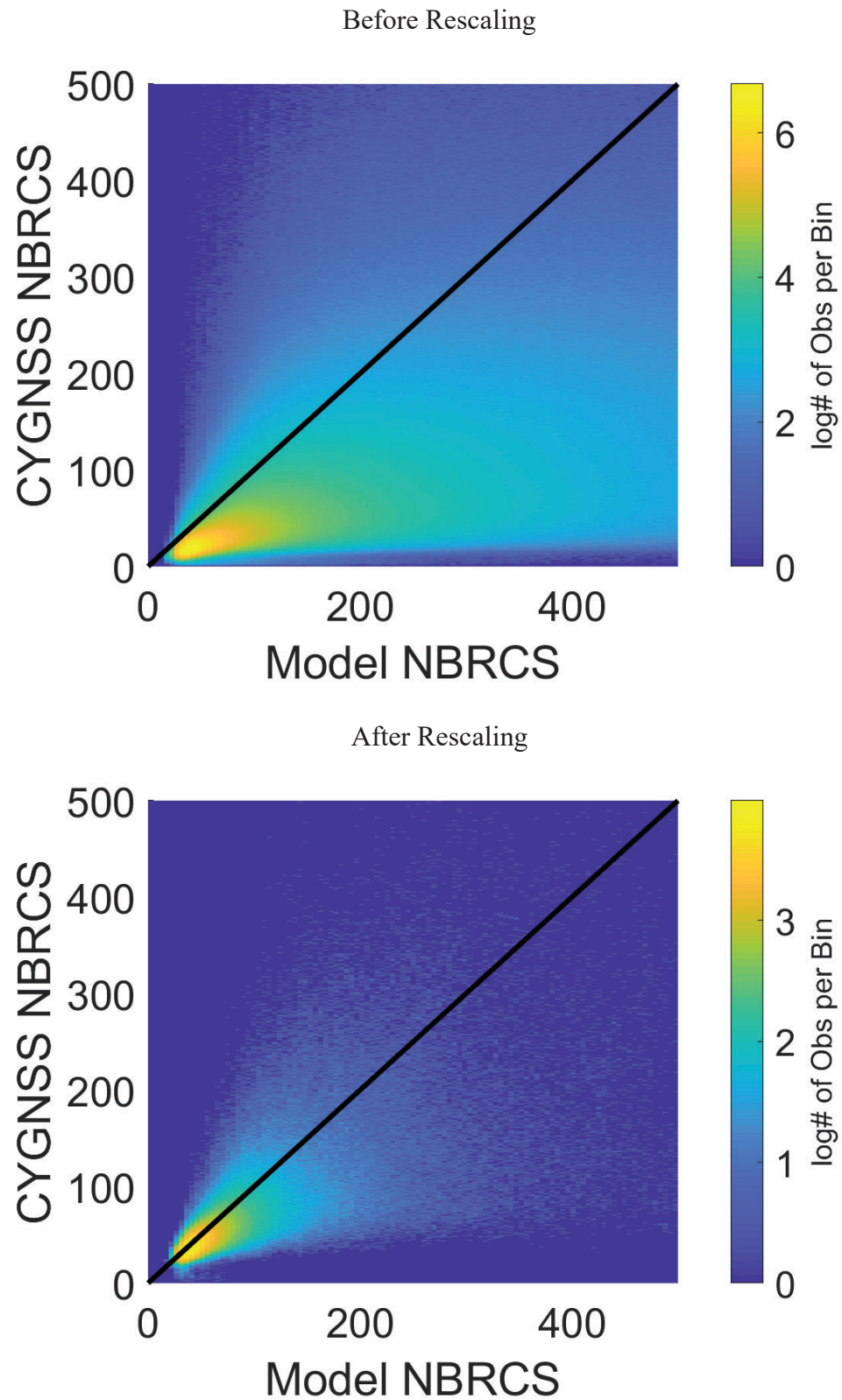
Before Rescaling

After Rescaling

Figure 14. Comparison of model based and CYGNSS NBRCS before (top) and after (bottom) antenna pattern rescaling.
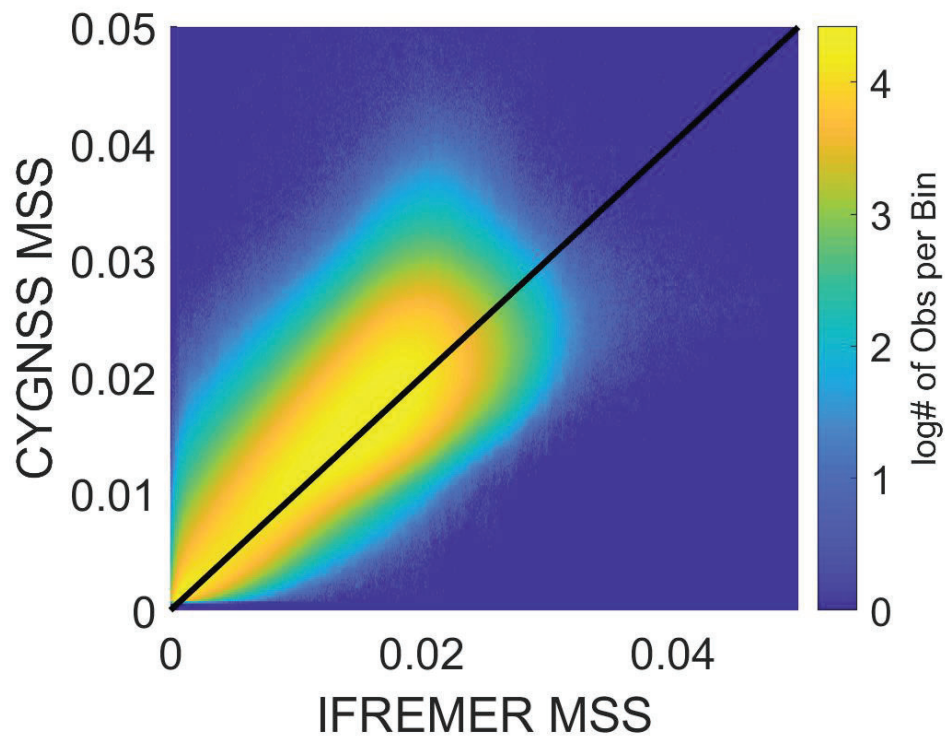
Figure 15. Comparison of model and CYGNSS MSS before (top) and after rescaling.
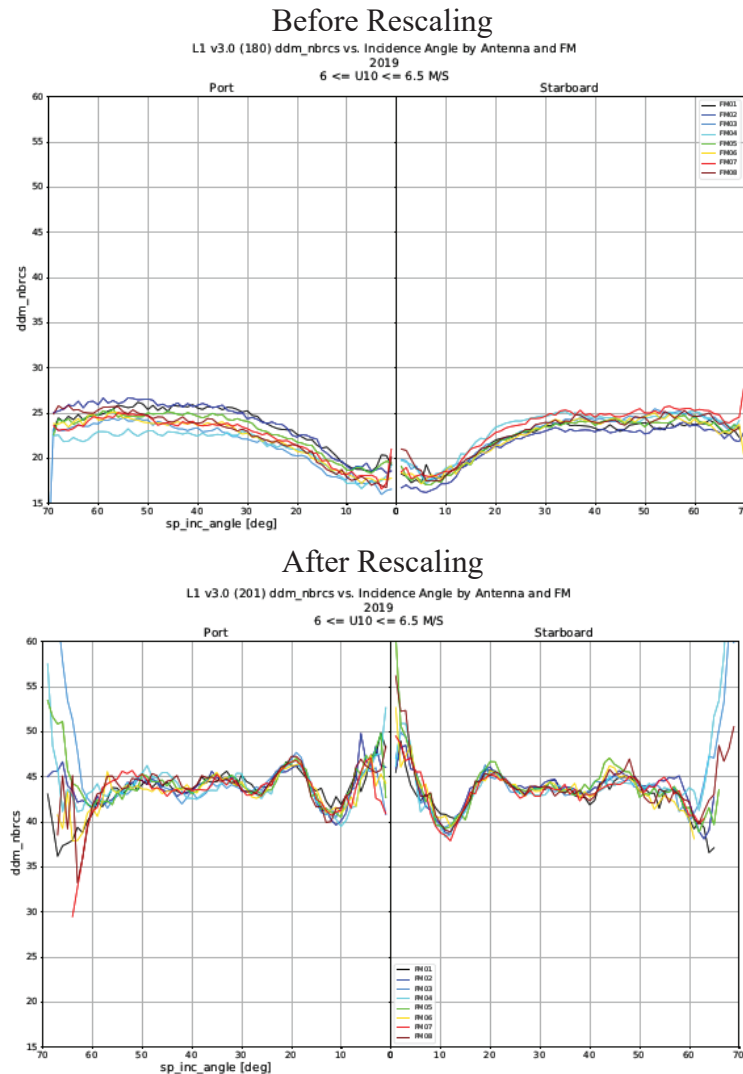
Figure 16. Mean NBRCS as a function of incidence angle for the starboard and port antennas of each FM before (top) and after (bottom) antenna pattern rescaling.

VI. CYGNSS LEVEL 1 ERROR ESTIMATION METHOD

This analysis assumes that the uncertainties in the CYGNSS Level 1 calibration algorithm are generally independent uncorrelated error sources, which can be characterized with a zero mean Gaussian distribution. This may not be strictly the case for some terms (most notably the GPS transmit power levels), yet to a first order this analysis serves to bound the expected error and as shown in the top-down analysis in Ruf et al [12] is consistent with the best estimate of the overall on-orbit observed CYGNSS wind retrieval performance. The method for this error analysis is based on the partial derivative method

presented in Jansen et. al [13]. Additionally, the rolled up error was simulated using a Monte Carlo simulation and was in agreement with the partial derivative estimated error levels presented below.

For more details on the partial derivatives for individual error terms in the L1a and L1b calibration equations refer to Gleason et al [5].

A. Error Analysis Methodology

The total error in the L1a or L1b calibrated DDM is the root of sum of squares (RSS) of the individual errors sources in the independent terms of their respective expressions, which can be expressed generically as,

$$\Delta L_1^{a,b} = \left[\sum_{i=1}^{x} [E(q_i)]^2 \right]^{1/2}$$

(11)

where $L_1^{a,b}$ are the L1a and L1b estimated error values, x is the number of independent errors terms and q_i are the respective input error parameters. The individual errors terms can be estimated by taking the partial derivatives of the calibration equation such that each error term in the process can by quantized as,

$$E(q_i) = \left| \frac{\partial L_1^{a,b}}{\partial q_i} \right| \Delta q_i$$

(12)

B. Rolled Up On-Orbit Level 1 Calibration Errors

The wrapped up errors of the Level 1b calibration can be expressed in a similar manner, with the total L1a error rolled in, and estimated over the DDMA region of the DDM (3 delays x 5 Dopplers),

$$\bar{\sigma}_{DDMA}^0 = \frac{P_{g,DDMA}(4\pi)^3 L_{atm}}{P^T \lambda^2 G_{SP}^T G_{SP}^R R_{SP}^{Total} A_{DDMA}}$$

(13)

Substituting this equation into Equation 12 results in,

$$E(q_i) = \left| \frac{\partial \bar{\sigma}_{DDMA}^0}{\partial q_i} \right| \Delta q_i$$

(14)

18

Where the errors terms are: $q_1 = P_g$ (rolled up L1a errors), $q_2 = DDMA_{crop}$, $q_3 = L_{atm}$, $q_3 = R_{SP}^{Total}$, $q_4 = P_T$, $q_5 = G^T$, $q_6 = G^R$ and $q_7 = A$, respectively.

The On-orbit estimated rolled up Level 1 calibration error is shown below II with 1-sigma error estimates for each term.

Error Term	Error Magnitude, dB	Comment
	At 10 m/s Reference Wind	
$E(P_g)$	0.13	Rolled Up L1a Error [14]
$E(DDMA_{crop})$	0.1	Error in DDMA Weighting Algorithm
$E(L_{atm})$	0.04	Atmospheric Losses
$E(R^{Total})$	2000 meters	Total range error

$E(P_T) + E(G^T)$	0.24	GPS Transmitter EIRP error from top-down analysis [12]
$E(G^R)$	0.25	Estimated Receiver Antenna Gain Error From MC Simulation
$E(A)$	0.05	Effective Scattering Area Error, From E2ES
Total RSS L1b Error, dB	0.39	Rolled Up L1b Error (Without Margin) From Partial Derivatives and MC Simulation

TABLE II. Rolled up Level 1B calibration error sources.

1) $E(P_g)$ is the rolled up L1a error from [14].

2) $E(DDMA_{crop})$ is an estimate of the error in the DDMA Weighting algorithm detailed above. The weighting algorithm uses a linear interpolation over non-linear DDM bins and this will introducs some error in the cropping of the final value. The value of 0.1 dB is an approximation based on ideal simulations of the DDMA weighting algorithm.

3) $E(L_{atm})$ is an estimate of the atmospheric attenuation over the signal path. Due to its L-band frequency, the atmospheric attenuation errors are expected to be very small [16].

4) $E(R^{Total})$ is the total error due to mis-estimation of the path loss from the GPS transmitter to the specular point to the receiver. Given the relatively high accuracies of all three of these parameters, this error is expected to be negligible. More details on the contribution due to the single frequency GPS receiver position estimation performed on CYGNSS can be found in [15].

5) $E(P_T) + E(G^T)$ is the error in the GPS transmit power and antenna gain correction. The best estimate for this error is based on analysis of the GPS Power Monitor determination of the GPS transmit powers [6] and the top down analysis reported in [12].

6) $E(G^R)$ is the error in the receive antenna gain and is based on the analysis of σ_0 anomalies described above, after the described corrections to the receive antenna patterns were applied. The antenna gain error was estimated using Monte Carlo simulations based on the predicted statistical spacecraft attitude performance and best estimate of the receive antenna gain pattern, described in more detail in [5].

7) $E(A)$ is the estimated error in the effective scattering normalization area used to convert σ to σ_0. The CYGNSS End-to-End Simulator was used to generate the look-up-tables used to generate these values. Given the extensive validation of the E2ES this error was at a relatively low value, driven by errors introduces due to the integration step size used in the table generation, plus a small amount of margin.

REFERENCES

[1] Gleason, S., Ruf, C.S., OBrien, A.J. and D.S. McKague, "The CYGNSS Level 1 Calibration Algorithm and Error Analysis Based on On-Orbit Measurements, " IEEE Journal of Selected Topics in Applied Earth Observation and Remote Sensing, 10.1109/JSTARS.2018.2832981, 2018.

[2] Zavorotny V. and A. Voronovich (2000), Scattering of GPS Signals from the Ocean with Wind Remote Sensing Application . IEEE Trans. Geosci. Remote Sens., Vol. 38, pp. 951-964, March 2000. DOI: 10.1109/36.841977

[3] DTU Space, National Space Instutute (Denmark). Global Mean Sea Surface.

[4] Bar-Sever, Y.,"A new model for GPS yaw attitude," Journal of Geodesy 70:714-723, 1996.

[5] Gleason, S., Ruf, C. Clarizia, M.P., OBrien, A. J.,"Calibration and Unwrapping of the Normalized Scattering Cross Section for the Cyclone Global Navigation Satellite System', IEEE Trans. Geoscience and Remote Sensing, Vol. 54, No. 5, May 2016.

[6] Wang, T., Ruf, C., Block, B., McKague, D. and S. Gleason, "Design and Performance of a GPS Constellation Power Monitor System for Improved CYGNSS L1B Calibration," IEEE Journal of Selected Topics in Applied Earth Observations and Remote Sensing, accepted for publication.

[7] W. A. Marquis, W.A. and D. L. Reigh, "The GPS Block IIR and IIR-M broadcast L-band antenna panel: Its pattern and performance, Navigation, vol. 62, no. 4, pp. 329-347, Dec. 2015.

[8] Wang, T., Ruf, C., Gleason, S., Block, B., McKague, D. and D. Provost, "Development of GPS constellation power monitor system for high accuracy calibration/validation of the CYGNSS L1B data, 2017 IEEE International Geoscience and Remote Sensing Symposium (IGARSS), Fort Worth, TX, pp. 1008-1011, July 23-28, 2017.

[9] Wang, T., Ruf, C., Block, B and D. McKague, "Characterization of the transmit power and antenna pattern of the GPS constellation for the CYGNSS mission, 2018 IEEE International Geoscience and Remote Sensing Symposium (IGARSS), Valencia, Spain, July 22-27, 2018.

19

[10] Steigenberger, P., Hauschild, A., Thoelert, S. and R. Langley, "US Air Force puts more power into GPS Block IIR-M C/A-code, GPS World, vol. 28, no. 4, pp. 8-9, Apr. 2017.

[11] Thoelert, S., Hauschild, A., Steigenberger, P. and R. Langley, "GPS IIR-M L1 transmit power redistribution: Analysis of GNSS receiver and highgain antenna data, Proceedings of the 30th International Technical Meeting of The Satellite Division of the Institute of Navigation, Portland, Oregon, Sept. 2017, pp. 1589-1602.

[12] Ruf, C.S., Gleason, S. and D.S. McKague, "Assessment of CYGNSS Wind Speed Retrieval Uncertainty," IEEE Journal of Selected Topics in Applied Earth Observation and Remote Sensing, 10.1109/JSTARS.2018.2825948, 2018.

[13] Jansen, M.A., Ruf, C.S. and S.J. Keihm (1995), TOPEX/Poseidon Mircorwave Radiometer (TMR): II. Antenna Pattern Correction and Brightness Temperature Algorithm, IEEE Trans. Geosci. Remote Sens., Vol. 33, No. 1, pp. 138-146, January 1995.

[14] Algorithm Theoretical Basis Document (ATBD): CYGNSS Level 1a DDM Calibration and Error Analysis, April 2018.

[15] Misra P., and P. Enge, Global Positioning System: Signals, Measurements, and Performance, Ganga Jamuna Press, 2001. ISBN 0-9709544-0-9.

[16] Ulaby, F. T., Long, D. G., Microwave Radar and Radiometric Remote Sensing, Ann Arbor, MI, USA: Univ. Michigan Press, 2014.

[17]